analytical chemistry

pubs.acs.org/ac

Article

Integrated System for On-Site Rapid and Safe Screening of COVID-19

Dongheyu Zhang,[▽] Yuntao Guo,[▽] Liyang Zhang, Yao Wang, Siqi Peng, Simeng Duan, Lin Geng, Xiao Zhang, Wei Wang, Mengjie Yang, Guizhen Wu, Jiayi Chen, Zihao Feng, Xinyuan Wang, Yue Wu, Haotian Jiang, Qikang Zhang, Jingjun Sun, Shenwei Li, Yuping He, Meng Xiao, Yingchun Xu,* Hongqiu Wang,* Peipei Liu,* Qun Zhou,* and Haiyun Luo*

Cite This: *Anal. Chem.* 2022, 94, 13810−13819

Read Online

ACCESS | Metrics & More | Article Recommendations | Supporting Information

ABSTRACT: Since the outbreak of coronavirus disease 2019 (COVID-19), the epidemic has been spreading around the world for more than 2 years. Rapid, safe, and on-site detection methods of COVID-19 are in urgent demand for the control of the epidemic. Here, we established an integrated system, which incorporates a machine-learning-based Fourier transform infrared spectroscopy technique for rapid COVID-19 screening and air-plasma-based disinfection modules to prevent potential secondary infections. A partial least-squares discrimination analysis and a convolutional neural network model were built using the collected infrared spectral dataset containing 857 training serum samples. Furthermore, the sensitivity, specificity, and prediction accuracy could all reach over 94% from the results of the field test regarding 968 blind testing samples. Additionally, the disinfection modules achieved an inactivation efficiency of 99.9% for surface and airborne tested bacteria. The proposed system is conducive and promising for point-of-care and on-site COVID-19 screening in the mass population.

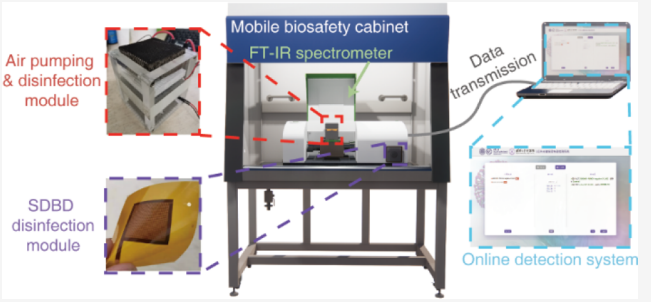

INTRODUCTION

Since December 2019,[1] the coronavirus disease 2019 (COVID-19), caused by a novel coronavirus named severe acute respiratory syndrome coronavirus 2 (SARS-CoV-2), has been continuously spreading and rapidly becoming a global pandemic as declared by the World Health Organization.[2] Although the specific vaccination coverage has been rising rapidly around the world, recent research has reported that the protection rate of vaccination could hardly reach 100%.[3−5] Hence, rapid and accurate population screening is still crucial for the control of COVID-19 spreading,[6,7] especially at airports or hospitals where large-scale screening is required. Optimal detection methods are expected to be on-site, rapid, simple, safe, and portable.[8,9]

For different detection targets and infection stages, conventional techniques for COVID-19 detection include reverse transcription polymerase chain reaction (RT-PCR) and serological antigen/antibody detection assay. The former aims at SARS-CoV-2 itself and the initial viral infection producing in the respiratory tract; therefore, the nasopharyngeal swab is mostly used as a detection sample. However, the latter focuses on the immune response occurring systemically in the whole body during the later stages of infection and the specific antibodies produced in the host serum. RT-PCR is the gold standard method for COVID-19 diagnosis but usually requires lengthy multi-step procession,[10] professional operations, and costly infrastructure.[11,12] Serological assays including chemiluminescence immunoassay (CLIA) and immunochromatography assay (ICA) are on the basis of antigen-/antibody-specific binding and considered to be complements to RT-PCR.[13,14] Serological assays usually show high specificity (81.25−99.00%) and sensitivity (81.00−100.00%),[15,16] especially at >7 days after symptom onset.[17] In addition, serological assays can help revealing the immune response in convalescents, vaccinated, or asymptomatic individuals.[18] Nevertheless, serological methods are susceptible to endogenous disruptors or nonspecific antibodies, resulting in false-positive results.[19] In addition, places such as airports may not be equipped with molecular diagnostic laboratories.[20,21] For methods such as PCR and CLIA, which require further operations in specialized laboratories, transportation process is unavoidable, making it difficult to achieve

Received: June 1, 2022
Accepted: September 22, 2022
Published: October 3, 2022

rapid on-site detection in some special situations, and antigen/antibody assays developed based on ICA, although they can give rapid test results, are statistically unreliable in terms of accuracy and have high costs for individual test equipment. The above limitations render the infeasibility of both methods in rapid and on-site COVID-19 detection.

It is the same category of method as CLIA and ICA to detect immune responses of infection, but unlike these two conventional assays which detect specific antigens or antibodies, vibrational spectroscopy technologies toward serum including attenuated total reflectance−Fourier transform infrared (ATR−FTIR) and Raman spectroscopy can monitor the changes in molecular compositions of serum,[22−24] yielding a "spectral fingerprint".[25] Vibrational spectroscopy has the advantages over traditional antibody test assays including less time-consuming, simplicity, no reagent, and lower exposure risk,[26] which has gained increasing interest in the diagnosis of infections caused by viruses such as dengue virus,[27] hepatitis B/hepatitis C,[28] herpes virus,[29] and human immunodeficiency virus.[30] Since the outbreak of COVID-19, ATR−FTIR has been preliminarily applied for COVID-19 detection. However, the existing reports are on a small sample scale of 57−250.[8,23,31−37] Thus, the applicability of this method on a larger sample scale requires verification. Furthermore, to achieve on-site COVID-19 detection, potential secondary infections to the environment and operators should be taken into consideration, although the viral load in the serum is low and not infectious.[38] Because given that spectroscopic methods have been applied in the detection of biological samples with high viral content such as saliva,[33] we envision that the new detection system may be used for more sample types in the future. In this regard, the potential emission of viable viruses should be minimized. Atmospheric pressure non-thermal plasma (APNTP) has been reported to effectively inactivate SARS-CoV-2 on surfaces.[39] Thus, APNTP can be incorporated to disinfect the air and surface of the operation space, achieving a safer detection process.

In this study, we report a mobile integrated system that is suitable for rapid and on-site COVID-19 screening, which can be used in places that include customs, hospitals, and so forth that are in large-scale infection screening demands but lack professional experimental conditions. Additionally, the integration of disinfection modules can reduce the requirements for laboratory biosafety levels compared with traditional methods. The effectiveness of FT-IR coupled with supervised machine learning models for COVID-19 detection was validated based on a dataset of 1702 spectra from 857 serum samples and examined by 968 on-site field tests. The results can be obtained from an online website minutes after sampling. The safety of the system was improved and guaranteed by two air-plasma-based modules for both air and surface disinfection.[40−42]

MATERIALS AND METHODS

Enrollment of Serum Samples and Measurement of FT-IR Spectra. The study was approved by Ethical review, and the sample collection procedure was conducted according to Novel Coronavirus Pneumonia Diagnosis and Treatment Guidance (Trial Version 8). Informed consent was obtained from all participants prior to blood collection. To be clear, all the participants have been collected only once for one sample.

Each inactivated serum sample was measured twice on a PerkinElmer infrared spectrometer coupled with an ATR accessory at a resolution of 4 cm^{-1} in a spectral range between 600 and 4000 cm^{-1}. The raw spectra collected were then preprocessed and differentiated using MATLAB (version R2020b, Mathworks, Natick, U.S.A), resulting in the second-derivative infrared (SD-IR) spectra. Details of measurements and data processing can be found in our previous study.[23]

Table 1 shows the components of the spectral dataset including 857 serum samples divided into 3 groups: (i) 511 positive samples for anti-SARS-CoV-2 IgG/IgM detected by CLIA, (ii) 149 healthy control samples, and (iii) 197 samples with negative anti-SARS-CoV-2 IgG/IgM but other immune diseases, which were treated as the interference ones. All serum samples were obtained from Peking Union Medical College Hospital and Shanghai International Travel Healthcare Center. Detailed information on each sample is provided in Data S1. In order to reduce the impact of operating errors, duplicate FT-IR spectra were obtained for each sample. Since some spectra with obvious errors were excluded, a total of 1702 available spectra from 857 samples were contained in the training dataset.

Table 1. Information on Serum Samples[a]

group	SARS-CoV-2 antibody testing results (CLIA)	serum samples	measured spectra
positive	(+)	511 (59.6%)	1010 (59.3%)
control	(−)	92 (10.7%)-cohort 1 57 (6.7%)-cohort 2	296 (17.4%)
interference	(−)	197 (23.0%)	396 (23.3%)
total		857	1702

[a]Cohort 1: collected in Peking Union Medical College Hospital. Cohort 2: collected in Shanghai International Travel Healthcare Center.

Parallel Antibody Testing of Serum Samples. Specific antibodies of SARS-CoV-2 in the serum samples were tested using two kinds of conventional serological assays, which were chemiluminescent immunoassay (CLIA) and colloidal gold immunochromatographic assay (GICA), respectively. After being incubated at 56 °C for 30 min to inactivate the potential viruses, the serum specimens were detected by an automatic CLIA analysis system (Beijing Wantai Biological Pharmacy Enterprise Co., Ltd., China) and a GICA kit (Beijing Innovita Biotechnology Co., Ltd., China or Shanghai Outdo Biotechnology Co., Ltd., China) parallelly. Since the sensitivity and specificity of CLIA are both significantly higher than those of GICA as reported,[16] we considered the CLIA as the standard for classification in the following study. Other routine immunological tests were performed on the CLIA-negative samples to distinguish between healthy controls and interferences further. Samples with abnormal immunological results were labeled interference since dysfunctional immune responses are common in clinical COVID-19 patients.[43]

PLS-DA and CNN Classification Models. In this study, two supervised pattern recognition algorithms were applied to distinguish between different groups of spectra, which were partial least-squares discriminant analysis (PLS-DA) and convolutional neural network (CNN), respectively. Implementation details of PLS-DA were explained in our previous work,[23] therefore is no more description here. Seventeen and 20 latent variables were selected in PLS-2C and PLS-3C, respectively (see Figure S1a,b).

https://doi.org/10.1021/acs.analchem.2c02337
Anal. Chem. 2022, 94, 13810−13819

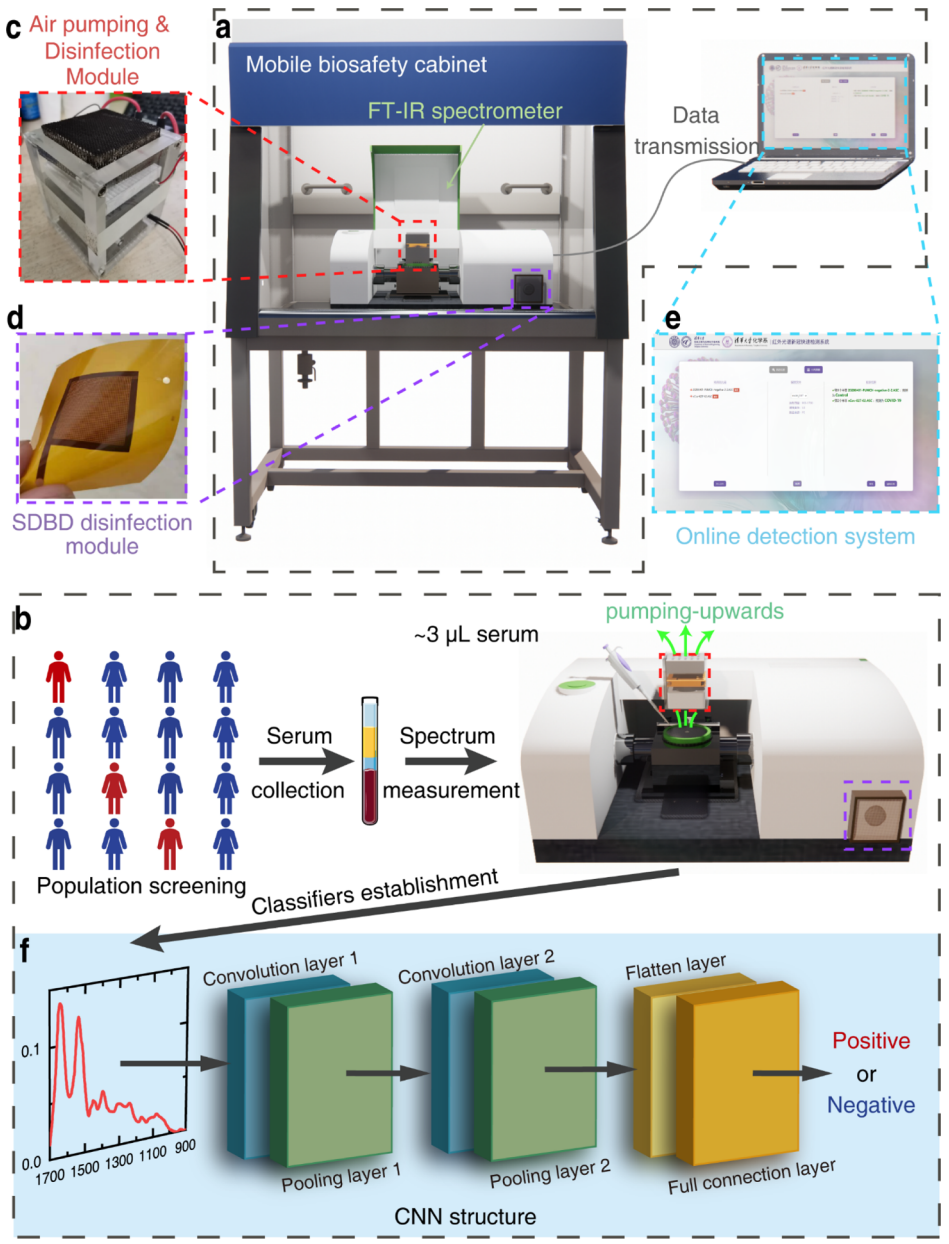

Figure 1. Integrated on-site screening system for COVID-19. (a) Schematic depicting the structure and essential components of the integrated on-site screening system for COVID-19. (b) Workflow of COVID-19 sample screening using the integrated on-site screening system. Details are presented in Materials and Methods section. (c) Design of air pumping and disinfection module. (d) Design of flexible disinfection film. (e) User interface of online FT-IR detection system for COVID-19 sera. (f) Structure of CNN.

CNN is a feedforward neural network, in which convolution is used instead of matrix multiplication in traditional neural networks.[44] The CNN models here were built using Python (3.6.4). The architecture of CNN consists of an initial input layer, followed by four hidden layers, a flatten layer, a fully connected classification layer, and a final output layer, as shown in the block diagram in Figure 1f. The four hidden layers are arranged alternately by two convolution layers (C1 and C2) and two pooling layers (P1 and P2), where C1 and C2 have 32 and 64 convolutional filters, respectively. Hyperparameters including the number of convolutional filters, the Kernel size, and the activation function were selected via pre-training using a small portion of the dataset. Before pre-training, the spectral dataset was randomly split into 70/30 train/validation groups. The performance of models with different hyperparameters were evaluated by training loss and classification accuracy on the validation split, both reported every five steps during training (see Figure S1c–f). In the final network, an Adam optimizer with a learning rate of 0.001, a straining step of 2000, and a batch size of 20 was applied across all experiments. Part of pre-training results is shown in Figures S2 and S3.

Same as the previous work, the present dataset was divided into three groups, which are named COVID-19, healthy control, and interference. In the present work, the data of the COVID-19 group and healthy control group were selected for training first, and the recognition models established based on the above two algorithms were named "PLS-2C" and "CNN-2C", respectively. Then, the interference group was added to the training set to explore the specificity of this method for

https://doi.org/10.1021/acs.analchem.2c02337
Anal. Chem. 2022, 94, 13810−13819

COVID-19 samples, and the two multi-classifiers were established and named "PLS-3C" and "CNN-3C". Here, the "1 versus else" method was adopted for each group separately, which means the sample of a certain group was coded as 1, and the others were coded as 0. As a result, the multi-classifier was converted into three binary classifiers.

10-Fold Cross-Validation. In order to compare the effectiveness of different classification models, 10-fold CV was used. The whole training dataset was randomly divided into 10 parts at first. In each iteration, only nine of them were used as the training set, and the remaining 1/10 as the validation set, which was repeated 10 times to obtain statistical results. Then, the evaluation indicators were calculated, including (i) sensitivity and specificity, (ii) receiver operating characteristic (ROC) curve, and area under the ROC curve (AUC).[45] The ROC curve was generated by calculating the sensitivity and specificity values under different decision thresholds.[46] The closer the ROC curve is to the upper-left edge, the higher the model accuracy is, and if it is below the diagonal, the model is considered invalid.

Disinfection Measures in the Operating Process. In the system, two plasma-based disinfection modules were integrated to avoid secondary infections during screening. One is an air pumping and disinfection module designed for the drying procession. As shown in Figure 1c, a plasma disinfection unit and a catalyst layer were integrated upon a pumping-upward fan, which kept the drying airflow in full contact with the discharge layer and disinfected by plasma before spreading to the surrounding space. Additionally, we constructed a flexible surface dielectric barrier discharge (SDBD) plasma film, whose detailed parameters can be found in our previous studies.[47] It can be pasted on the surface of the spectrometer button to achieve in situ disinfection (Figure 1d). The module can discharge under a relatively low voltage with an amplitude of 2.0−3.0 kV. The voltage and current waveform are shown in Figure S1, and the discharge power is only 0.2−0.5 W.

Efficiency Evaluation of the Air Pumping and Disinfection Module. The test for the air pumping and disinfection module was carried out in a pair of sealed aerosol chambers (1 m^3). The temperature and relative humidity were 25 °C and 50−70%. According to the Technical Specifications for Disinfection (2002 edition), two identical microbial aerosol generators were used to spray *Staphylococcus albus* into both chambers at the same time, and the spraying, mixing, and standing time were 5 min, respectively. After the polluted environment was set up, bacteria were sampled by six-stage Anderson cascade impactors with a flow rate of 28.3 L/min before and after 30 min of plasma disinfection. The sampling time before disinfection was 5 s and that after disinfection was 1 min. The plates were incubated at 37 °C for 24 h and then counted the colony-forming unit (CFU) of the bacteria. The airborne bacterial concentration is calculated by

$$V = \frac{S}{28.3t} \times 1000$$

where V is the airborne bacterial concentration (CFU/m^3), S is the total CFU number in the sampling plates (CFU), and t is the sampling time (min).

The disinfection effect of the module K is calculated by

$$N = \frac{V_0 - V_t}{V_0} \times 100$$

$$K = \frac{V_0'\left(1 - \frac{N}{100}\right) - V_t'}{V_0'\left(1 - \frac{N}{100}\right)} \times 100$$

where N is the natural survival decaying percent of bacterial aerosols, V_0 and V_t are the airborne bacterial concentration of the control group during the experiment, K is the inactivation rate of airborne bacteria caused by plasma disinfection treatment, V_0' and V_t' are the airborne bacterial concentration before and after plasma disinfection treatment, respectively.

Efficiency Evaluation of the Flexible SDBD Disinfection Film. In order to verify the surface disinfection effect, the film was infected with *Escherichia coli* to simulate a pollutant surface. The bacterial suspension concentration is 1×10^8 CFU/mL, 100 μL of which was dripped onto the discharge area (4 cm^2) and then dried by a fan for 1 h. After the plasma disinfection, the film was transferred to a 5 mL sterile centrifuge tube (pre-added with 2 mL eluent), and the bacteria on the film were eluted using an electric mixer for 5 min. Then, the bacteria were serially diluted and incubated at 37 °C for 24 h and then counted the CFU of the bacteria. Finally, quantitative disinfection effect is calculated as log reduction. Simultaneously, the same operations were performed on uncontaminated disinfection films as the negative control group and films contaminated with bacterial suspension but without plasma treatment as a positive control group.

Field Blind Test of COVID-19 Screening. Afterward, over 968 samples (2005 FT-IR spectra obtained) were collected by the integrated system in Shanghai International Travel Healthcare Center and Peking Union Medical College Hospital, and these samples were used to conduct a blind clinical test of the system. All the patients and samples for blind testing were not included in the training set, and there was no case where two or more samples came from the same patient.

Information on the testing samples can be found in Data S2. Same as the training samples, parallel antibody tests (CLIA) were operated to determine the class of testing sera.

RESULTS

Design of the Integrated On-Site Screening System for COVID-19. The integrated on-site screening system was established upon our preliminary study,[23] which showed the feasibility of FT-IR coupled with multi-variate analysis for fast COVID-19 screening. The proposed system combined four main modules (Figure 1a): (i) a mobile biosafety cabinet used to prevent the emission of potential pathogens, (ii) an ordinary ATR−FTIR spectrometer used to collect the mid-infrared spectra of the serum samples, and (iii) a computer that is connected to the homemade online software named online FT-IR detection system for COVID-19 sera, by which positive spectra can be identified. Briefly, the spectra are first collected by the FT-IR spectrometer. Then, the spectral data are manually uploaded to the online software, and the built-in recognition models can give the classification results in tens of seconds (Figure 1e). (iv) Air pumping and disinfection module (Figure 1c), which is placed above the sample on the ATR accessory. The module consists of a fan, an air plasma disinfector, and a catalytic panel. The fan is used to draw the surrounding air around the sample through the module to accelerate sample drying. The plasma reactor is applied to inactivate the potential viral aerosol generated during sample drying processes. The catalytic panel is used to reduce the

https://doi.org/10.1021/acs.analchem.2c02337
Anal. Chem. 2022, 94, 13810−13819

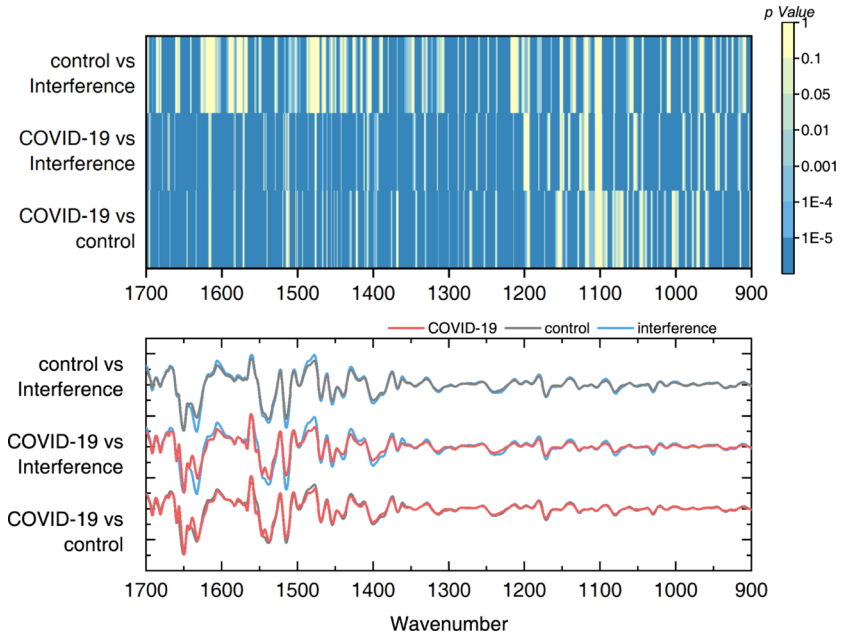

Figure 2. ANOVA results for the average spectra of each group. (a) p values of in-pair average spectra at each wavenumber. The darker blue grids represent the lower p values at the corresponding wavenumbers. Spectral differences were statistically significant when $p < 0.0001$. (b) Direct comparison in pairs of the three average in-group SD spectra. The visible differences shown here are consistent with the p values above.

Table 2. Performance of Classifiers (ROC Curves and 10-Fold Cross-Validation Accuracies)

method	group	threshold	sensitivity (%)	specificity (%)	AUC (95% CI)	accuracy (%) for CV
PLS-2C	COVID-19	0.62	98.53	98.81	0.9986 (0.9971−0.9993)	99.41
	control					91.20
			Overall Accuracy (%)			97.09
CNN-2C	COVID-19	0.46	99.66	99.00	0.9998 (0.9992−1.000)	98.95
	control					87.01
			Overall Accuracy (%)			96.24
PLS-3C	COVID-19	0.62	97.73	96.40	0.9923 (0.9874−0.9953)	99.11
	control	0.44	81.91	96.17	0.9673 (0.9578−0.9753)	73.59
	interference	0.49	92.95	95.92	0.9900 (0.9866−0.9927)	90.40
			Overall Accuracy (%)			91.46
CNN-3C	COVID-19	0.89	99.72	99.29	0.9999 (0.9996−1.000)	99.02
	control	0.22	97.15	98.79	0.9980 (0.9963−0.9990)	96.78
	interference	0.78	96.13	99.70	0.9992 (0.9985−0.9997)	95.02
			Overall Accuracy (%)			97.63

ozone emission from the plasma reactor to a safe level. (v) Surface disinfection module (Figure 1d), which is tightly attached to the buttons of the infrared spectrometer to avoid the potential surface contamination of the virus. The module is a SDBD disinfector based on a flexible printed circuit technique.[48]

Notably, the virus is rare in serum, but it may exist in other specimens such as throat swabs, nasal swabs, and so forth. Thus, the proposed system is also safe in terms of COVID-19 screening using other biological analytes. The whole on-site and real-time detection processes are shown in Figure 1b.

Analysis of Variance for the Average Spectra of Each Group. All the spectra were labeled COVID-19, healthy control, and interference and divided into three groups according to the results of CLIA and other serological tests. One-way analysis of variance (ANOVA) was applied to evaluate the difference in the SD-IR spectra between groups.[23] The average spectra of each group were compared in pairs (Figure 2b). Also, the p values at each wavenumber were calculated (Figure 2a). The most pronounced distinction between groups arises in the protein IR region (1700−1480 cm^{-1})[49] as suggested by both the p value results and the direct comparison of spectra, which is consistent with the serum composition changes in COVID-19 patients from previous reports (see Table S1).

Differentiating COVID-19 from Other Samples Based on PLS-DA and CNN Classifiers. *Positive Control Classifiers.* To further differentiate the COVID-19-positive and healthy control samples, two categories of binary classifiers, named PLS-2-Classifier (PLS-2C) and CNN-2-Classifier (CNN-2C), were established based on PLS-DA and CNN algorithms, respectively. The training data here contains a total of 1306 spectra, 1010 of which are from COVID-19 patients and 296 from healthy controls (Table 1). To evaluate the model performance, 10-fold cross-validation (CV) was used[50] to get the model prediction accuracies (see the last column in Table 2), and the ROC curves were generated by disturbing the threshold. The AUC of PLS-2C was 0.9986

https://doi.org/10.1021/acs.analchem.2c02337
Anal. Chem. 2022, 94, 13810−13819

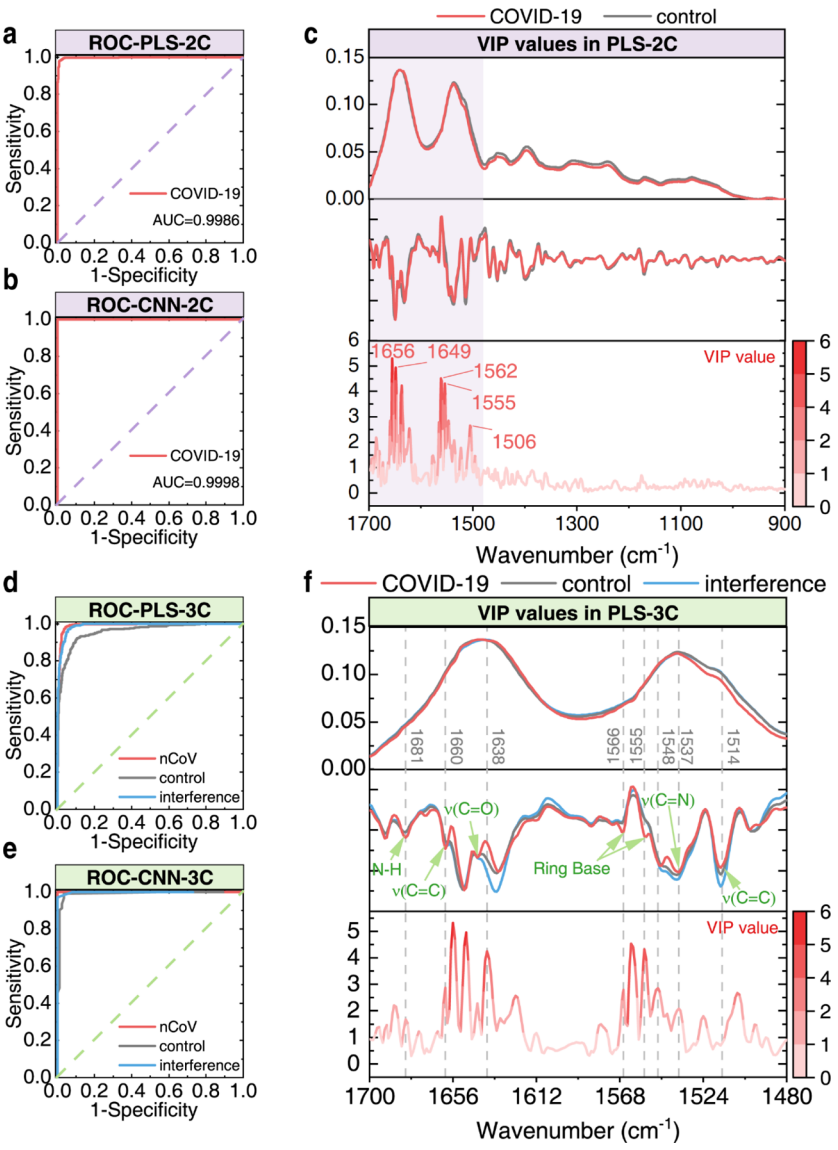

Figure 3. Evaluation results of classification models. (a) ROC of COVID-19 samples obtained from PLS-2C. (b) ROC of COVID-19 samples obtained from CNN-2C. (c) Regression vector of COVID-19 from PLS-2C with respect to the spectral region of 1700−900 cm^{-1}. VIP values reflect the importance of specific spectral regions. (d) ROCs of three groups of samples obtained from PLS-3C. (e) ROCs of three groups of samples obtained from CNN-3C. (f) Regression vector of COVID-19 from CNN-2C with respect to the spectral region of 1700−1480 cm^{-1}.

(95% CI: 0.9971−0.9993) (Figure 3). With an optimal threshold, sensitivity and specificity of PLS-2C could reach 98.53 and 98.81% (threshold set as 0.3661). Meanwhile, the CNN-2C model yielded an AUC value of 0.9998 (95% CI: 0.9992−1.0000) and the sensitivity and specificity values of 99.66 and 99.00%, respectively. Overall, the performance of CNN-2C was a bit better than that of PLS-2C. All detailed results of CV are shown in Table 2.

The variable importance in the projection (VIP)[51] values are presented in Figure 3. Apparently, the most important bands for discrimination are located at 1656, 1649, 1638, 1562, 1555, and 1506, within the amide region (1700−1500 cm^{-1}).

Multi-classifiers Including the Interference Group. In practice, antibody detection methods such as CLIA and GICA can be disturbed by various existing interfering substances[11] in serum and autoimmune disease,[19] which is possible to increase the false-positive rate. The used IR method may also have the problem of false positives. Therefore, we additionally collected serum samples with abnormal immune levels but negative SARS-CoV-2 antibody results as interference. Two multi-classifiers named PLS-3C and CNN-3C were established to evaluate the specificity of the detection using the expanded dataset containing 1702 IR spectra (Table 1). The establishment and training process of the multi-classifiers were identical to the binary classifiers.

The same evaluation methods with the binary classifiers were applied to PLS-3C and CNN-3C. As described in Materials and Methods section, ROCs presented in Figure 3d,e were obtained for each class respectively by disturbing the classification thresholds. As shown in the PLS-3C results in Table 2, the highest AUC value of 0.9923 (95% CI: 0.9874−0.9953) and the highest accuracy of 99.21% are from the COVID-19 vs other two groups. The AUC values for interference and healthy control are 0.9900 (95% CI: 0.9866−0.9927) and 0.9673 (95% CI: 0.9578−0.9753), respectively, while the prediction accuracy values of the interference and control groups are 93.20 and 72.86%, much lower than the COVID-19 group. Compared with the PLS-3C

https://doi.org/10.1021/acs.analchem.2c02337
Anal. Chem. 2022, 94, 13810−13819

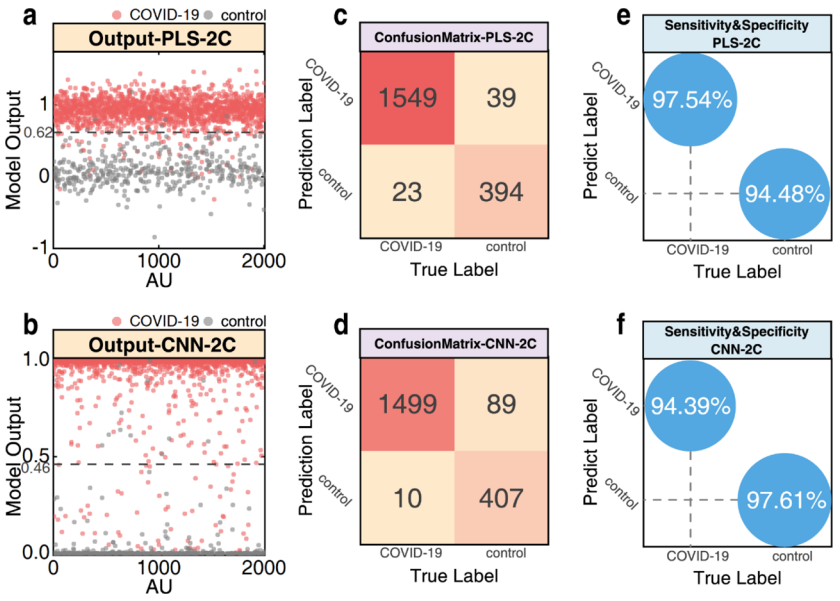

Figure 4. Statistical results of field blind test at Shanghai customs. (a) Model output of PLS-2C. The direct output represents the probability of being positive given by the classifier. (b) Model output of CNN-2C. (c) Confusion matrix of classification results obtained from PLS-2C. (d) Confusion matrix of classification results obtained from CNN-2C. (e) Confusion ball visualization of sensitivity (true positive) and specificity (true negative) obtained from PLS-2C. (f) Confusion ball visualization of sensitivity (true positive) and specificity (true negative) obtained from CNN-2C.

Table 3. Disinfection Results of Air Pumping Module

no.	bacterial number of control group at 0 min (CFU/m^3)	bacterial number of control group at 30 min(CFU/m^3)	natural survival decaying percent (%)	bacterial number of experimental group at 0 min (CFU/m^3)	bacterial number of experimental group at 30 min (CFU/m^3)	inactivation rate (%)
1	105 265	104 735	0.50	109 187	155	99.9
2	104 841	94 982	9.40	104 099	106	99.9
3	96 784	74841	22.67	138 551	92	99.9

results, the performance of CNN-3C improved significantly, where the AUC and prediction accuracy values of the three groups are all above 0.9900 and 97.00%. Namely, CNN-3C is superior to PLS-3C in interference and control identification.

Results of Field Blind Test at Shanghai Customs. Following training and validation of the binary classifiers, field blind tests were carried out on site at Shanghai customs. A total of 968 blind serum samples were obtained. From the output of the two models shown in Figure 4a,b, it was found that most of the testing data could be distinctly separated. The comparison between the results from FT-IR and CLIA is shown in confusion matrixes (CMs) in Figure 4c,d, where CLIA results are used as the references. The entry (i, j) represents the number of tested spectra predicted as class j at a given true CLIA label of class i, while entries along the diagonal represent the accurate numbers for each class. Calculating from the CMs, both PLS-2C and CNN-2C reached a high prediction accuracy of 96.91 and 95.06%, respectively, which are comparable to that of the commonly used commercial serological COVID-19 assays. Besides, PLS-2C has a higher sensitivity value of 97.54%, while CNN-2C has a higher specificity value of 97.60%.

EFFICIENCY EVALUATION OF PLASMA-BASED DISINFECTION MODULES

Air Pumping and Disinfection Module. SARS-CoV-2 is a kind of lipophilic virus surrounded by an envelope, which makes it the most easily inactivated type among microorganisms and can be eliminated with the least effective disinfectant.[52] Bacteria are more resistant to disinfection methods. Therefore, in order to verify the disinfection effect of the system on various pathogens, we selected *S. albus* as the disinfecting target to simulate the polluted environment for the field experiments.

S. albus (ATCC 8032) aerosol was sprayed into the experimental chambers to simulate the polluted air, and the disinfection ability of the air pumping and disinfection module was evaluated (see Materials and Methods section for details). The results are shown in Table 3. The *S. albus* inactivation rate of this module could reach higher than 99.9% in the experimental chamber of 1 m^3 after working for 30 min. The air disinfection effect is qualified according to disinfection technical specification.

Flexible SDBD Disinfection Film. *E. coli* suspension was dripped onto the flexible film to simulate the contaminated surface, and the performance of the flexible SDBD disinfection film was simulated and tested. The results are given in Table 4. The Log reduction of surviving *E. coli* can reach 3.29 after 10 min of plasma treatment. The surface disinfection effect is qualified.

DISCUSSION

Innovations of This Work. In recent two years, FT-IR or Raman spectroscopy has been suggested for COVID-19 detection using serum samples,[35,36] prediction of COVID-19 disease severity using plasma samples,[34] SARS-CoV-2

https://doi.org/10.1021/acs.analchem.2c02337
Anal. Chem. 2022, 94, 13810−13819

Table 4. Disinfection Results of Flexible Plasma Film

no.	log value of control group	log value of experimental group	log reduction	average value
1	5.20	1.82	3.38	3.29
2	5.18	1.52	3.66	
3	5.26	2.43	2.83	

detection in saliva,[33] and so forth (summarized in Table 2). The sample scales in previous reports are usually about 80−250, which is much lower than that in the present work of 1825 samples, of which 857 for training and 968 for field blind testing. In our previous report,[23] a total of 115 serum samples were enrolled to establish PLS-DA models for COVID-19 screening. The AUC value achieved 0.9561 (95% CI: 0.9071−0.9774) when considering the patients with respiratory viral infections or inflammation-related diseases. In the present work, the larger sample scale of 857 resulted in a better performance of the classification models. High AUC values of 0.9986 (95% CI: 0.9971−0.9993) and 0.9923 (95% CI: 0.9874−0.9953) were obtained by PLS-2C and PLS-3C models, respectively, again demonstrating the applicability of this method.

On the basis of the larger dataset, the neural network CNN was first built in this work for COVID-19 detection using spectral data rather than conventionally used images. As mentioned in the Results section, for binary classification, both PLS-2C and CNN-2C classifiers achieved good performance. The sensitivity and specificity values of CNN-2C are only slightly higher than those of PLS-2C. In terms of the multi-class classification, CNN-3C yields a higher specificity for the COVID-19 group than that of PLS-3C (99.29% > 96.40%, Table 2). Namely, compared to the CNN-based model, the PLS-DA-based model is more easily affected by interferences. The highly nonlinear characteristic of CNN could explain such a result.[53] However, CNN has the disadvantage of insufficient interpretability. The key wavenumbers or spectral features for COVID-19 identification are difficult to find out. Concerning the field test at Shanghai customs, CNN-2C showed a relatively lower sensitivity value than PLS-2C, possibly due to the imbalanced data distribution in the training data.[54] Of all the training data (1702 items), the healthy control group (296 items) only accounts for 17.4%, below a quarter of the total number. Inadequate feature extraction of data is prone to suffer from overfitting, which leads to poor generalization ability of the classifier. Continued expansion of the data scale or oversampling the vulnerable groups is required in the future work. Overall, the combination of FT-IR technology with complex deep learning networks shows great potential for accurate COVID-19 diagnosis and is also promising for the diagnosis of other diseases.

The field test in this study was performed using an integrated system (Figure 1a), which is mobile and easy to transport. To reduce the operation complexity, an online system (Figure 1e) was developed to assist the operator to access the detection result as soon as possible. The detected spectral data uploaded to the website will be recorded and added to the whole database if with the permission from testees. With the integration of a cabinet, a spectrometer, an online software, and disinfection modules, the whole detection process including spectral acquisition, data analysis, and identification can be accomplished by a single system.

Limitations of This Work. As stated in the Introduction section, optimal detection methods are expected to be on-site, rapid, simple, safe, and portable. In this case, non-invasive samples may be more suitable for field testing, such as a fingerpick of whole blood. However, whole blood contains complex components including serum and blood cells, and the detection of whole blood samples by spectroscopic methods can be strongly interfered by other components, which can seriously affect the identification results. In contrast, serum has a simpler composition, and the detection of immune infection target substances is more significant and more accurate. Therefore, serum was used as the target in this study, and the separation process of serum is unavoidable. This is a limitation of the FT-IR methodology, but still, it cannot be denied that the new system has unique advantages over other serological assays. Under the same pre-treatment conditions requiring serum separation, the system can reduce the detection time of a single sample from 3 to 4 h to less than 10 min compared to CLIA and can achieve a higher level of accuracy in the same time consumption as GICA.

There have been preliminary studies in the literature on non-invasive saliva samples for SARS-CoV-2 detection in the early stage of infection. However, while for the systemic immune responses in the later stages of infection, all studies consistently use isolated serum or plasma instead of whole blood, indicating that whole blood itself is difficult to be analyzed thoroughly by IR spectroscopy. In the future, other methods can be explored to achieve direct detection of fingertip blood to further save processing time and cost.

CONCLUSIONS

A mobile integrated system was proposed and established in this work for on-site detection of COVID-19. The effective identification of COVID-19 using ATR FTIR spectroscopy technology was fulfilled by two machine learning models based on a spectral dataset containing 1702 spectra and validated by 968 field tests, which achieved a prediction accuracy of >94% both in the positive and healthy control group, respectively. The whole detection process can be completed in minutes. Besides, the air and surface disinfection modules based on atmospheric pressure plasmas were established to guarantee the operational safety of the system. The proposed system is expected as a powerful supplement to the current laboratory-based COVID-19 diagnosis, especially in cases requiring mass population screening.

ASSOCIATED CONTENT

Supporting Information

The Supporting Information is available free of charge at https://pubs.acs.org/doi/10.1021/acs.analchem.2c02337.

Training process of classifiers; changes of classification accuracy and model loss values over learning rate after 100 training iterations; curves of classification accuracy and model loss values in the training of the CNN which contained three convolution layers and three pooling layers; summary of composition changes in the serum of patients with COVID-19; and comparison of FT-IR results (PDF)

Detailed information of training serum samples mentioned in the table (XLSX)

Detailed information of blind testing serum samples (XLSX)

https://doi.org/10.1021/acs.analchem.2c02337
Anal. Chem. 2022, 94, 13810−13819

AUTHOR INFORMATION

Corresponding Authors

Yingchun Xu − *Department of Clinical Laboratory, Peking Union Medical College Hospital, Chinese Academy of Medical Sciences, Beijing 100730, China*; Email: xycpumch@139.com

Hongqiu Wang − *JINSP Co., Ltd., Beijing 100083, China*; Email: wanghongqiu@jinsp-tech.com

Peipei Liu − *Chinese Center for Disease Control and Prevention, National Institute for Viral Disease Control and Prevention, Beijing 102206, China*; Email: liupp@ivdc.chinacdc.cn

Qun Zhou − *Department of Chemistry, Tsinghua University, Beijing 100084, China*; Email: zhouqun@tsinghua.edu.cn

Haiyun Luo − *Department of Electrical Engineering, Tsinghua University, Beijing 100084, China*; Email: lhy@tsinghua.edu.cn

Authors

Dongheyu Zhang − *Department of Electrical Engineering, Tsinghua University, Beijing 100084, China*; orcid.org/0000-0001-6912-195X

Yuntao Guo − *Department of Electrical Engineering, Tsinghua University, Beijing 100084, China*

Liyang Zhang − *Department of Electrical Engineering, Tsinghua University, Beijing 100084, China*; orcid.org/0000-0001-9909-9263

Yao Wang − *Department of Clinical Laboratory, Peking Union Medical College Hospital, Chinese Academy of Medical Sciences, Beijing 100730, China*

Siqi Peng − *Department of Electrical Engineering, Tsinghua University, Beijing 100084, China*; orcid.org/0000-0001-5418-3656

Simeng Duan − *Department of Clinical Laboratory, Peking Union Medical College Hospital, Chinese Academy of Medical Sciences, Beijing 100730, China*

Lin Geng − *JINSP Co., Ltd., Beijing 100083, China*

Xiao Zhang − *JINSP Co., Ltd., Beijing 100083, China*

Wei Wang − *Shanghai Customs Port Clinic, Shanghai International Travel Healthcare Center, Shanghai 200335, China*

Mengjie Yang − *Chinese Center for Disease Control and Prevention, National Institute for Viral Disease Control and Prevention, Beijing 102206, China*

Guizhen Wu − *Chinese Center for Disease Control and Prevention, National Institute for Viral Disease Control and Prevention, Beijing 102206, China*

Jiayi Chen − *Department of Electrical Engineering, Tsinghua University, Beijing 100084, China*

Zihao Feng − *Department of Electrical Engineering, Tsinghua University, Beijing 100084, China*

Xinyuan Wang − *Holy-shine Technology Co., Ltd., Beijing 100045, China*

Yue Wu − *Holy-shine Technology Co., Ltd., Beijing 100045, China*

Haotian Jiang − *Department of Electrical Engineering, Tsinghua University, Beijing 100084, China*

Qikang Zhang − *Department of Electrical Engineering, Tsinghua University, Beijing 100084, China*

Jingjun Sun − *Department of Electrical Engineering, Tsinghua University, Beijing 100084, China*

Shenwei Li − *Shanghai Customs Port Clinic, Shanghai International Travel Healthcare Center, Shanghai 200335, China*

Yuping He − *Shanghai Customs Port Clinic, Shanghai International Travel Healthcare Center, Shanghai 200335, China*

Meng Xiao − *Department of Clinical Laboratory, Peking Union Medical College Hospital, Chinese Academy of Medical Sciences, Beijing 100730, China*

Complete contact information is available at: https://pubs.acs.org/10.1021/acs.analchem.2c02337

Author Contributions

$^{\nabla}$D.Z and Y.G contributed equally.

Notes

The authors declare no competing financial interest.

ACKNOWLEDGMENTS

This work was funded by the Tsinghua University Spring Breeze Fund (2020Z99CFG007), the Tsinghua University Peking Union Medical College Hospital Initiative Scientific Research Program (20191080604), the China Postdoctoral Science Foundation (2021M701945), the National Key Research and Development Program of China (no. 2020YFC0862100), and the State Key Laboratory of Power System Operation and Control (SKLD22KM03).

REFERENCES

(1) Zhou, P.; Yang, X. L.; Wang, X. G.; Hu, B.; Zhang, L.; Zhang, W.; Si, H.-R.; Zhu, Y.; Li, B.; Huang, C.-L.; Chen, H.-D.; Chen, J.; Luo, Y.; Guo, H.; Jiang, R.-D.; Liu, M.-Q.; Chen, Y.; Shen, X.-R.; Wang, X.; Zheng, X.-S.; Zhao, K.; Chen, Q.-J.; Deng, F.; Liu, L.-L.; Yan, B.; Zhan, F.-X.; Wang, Y.-Y.; Xiao, G.-F.; Shi, Z.-L. *Nature* **2020**, *579*, 270−273.

(2) Cucinotta, D.; Vanelli, M. *Acta Bio Med. Atenei Parmensis* **2020**, *91*, 157.

(3) Dagan, N.; Barda, N.; Kepten, E.; Miron, O.; Perchik, S.; Katz, M. A.; Hernán, M. A.; Lipsitch, M.; Reis, B.; Balicer, R. D. *N. Engl. J. Med.* **2021**, *384*, 1412−1423.

(4) Zhang, Y.; Zeng, G.; Pan, H.; Li, C.; Hu, Y.; Chu, K.; Han, W.; Chen, Z.; Tang, R.; Yin, W.; Chen, X.; Hu, Y.; Liu, X.; Jiang, C.; Li, J.; Yang, M.; Song, Y.; Wang, X.; Gao, Q.; Zhu, F. *Lancet Infect. Dis.* **2021**, *21*, 181−192.

(5) Stephenson, K. E.; Le Gars, M.; Sadoff, J.; de Groot, G.; Heerwegh, M.; Truyers, D.; Atyeo, C.; Loos, C.; Chandrashekar, C.; McMahan, A.; Tostanoski, K.; Yu, J.; Gebre, M. S.; Jacob-Dolan, C.; Li, Z.; Patel, S.; Peter, L.; Liu, J.; Borducchi, E. N.; Nkolola, J. P.; Souza, M.; Tan, C. S.; Zash, R.; Julg, B.; Nathavitharana, R. R.; Shapiro, R. L.; Azim, A. A.; Alonso, C. D.; Jaegle, K.; Ansel, J. L.; Kanjilal, D. G.; Guiney, C. J.; Bradshaw, C.; Tyler, A.; Makoni, T.; Yanosick, K. E.; Seaman, M. S.; Lauffenburger, D. A.; Alter, G.; Struyf, F.; Douoguih, M.; Van Hoof, J.; Schuitemaker, H.; Barouch, D. H. *JAMA, J. Am. Med. Assoc.* **2021**, *325*, 1535−1544.

(6) Premraj, A.; Aleyas, A. G.; Nautiyal, B.; Rasool, T. J. *Diagnostics* **2020**, *10*, 866.

(7) Lu, S.; Tong, X.; Han, Y.; Zhang, K.; Zhang, Y.; Chen, Q.; Duan, J.; Lei, X.; Huang, M.; Qiu, Y.; Zhang, D.-Y.; Zhou, X.; Zhang, Y.; Yin, H. *Nat. Biomed. Eng.* **2022**, *6*, 286−297.

(8) Huang, J.; Wen, J.; Zhou, M.; Ni, S.; Le, W.; Chen, G.; Wei, L.; Zeng, Y.; Qi, D.; Pan, M.; Xu, J.; Wu, Y.; Li, Z.; Feng, Y.; Zhao, Z.; He, Z.; Li, B.; Zhao, S.; Zhang, B.; Xue, P.; He, S.; Fang, K.; Zhao, Y.; Du, K. *Anal. Chem.* **2021**, *93*, 9174−9182.

(9) Ning, B.; Yu, T.; Zhang, S.; Huang, Z.; Tian, D.; Lin, Z.; Niu, A.; Golden, N.; Hensley, K.; Threeton, B.; Lyon, C. J.; Yin, X. M.; Roy, C.

J.; Saba, N. S.; Rappaport, J.; Wei, Q.; Hu, T. Y. *Sci. Adv.* **2021**, *7*, No. eabe3703.
(10) Wu, Q.; Suo, C.; Brown, T.; Wang, T.; Teichmann, S. A.; Bassett, A. R. *Sci. Adv.* **2021**, *7*, No. eabe5054.
(11) Jing, R.; Kudinha, T.; Zhou, M. L.; Xiao, M.; Wang, H.; Yang, W. H.; Xu, Y. C.; Hsueh, P. R. *J. Microbiol., Immunol. Infect.* **2021**, *54*, 17−26.
(12) Li, H.; Yang, J.; Wu, G.; Weng, Z.; Song, Y.; Zhang, Y.; Vanegas, J. A.; Avery, L.; Gao, Z.; Sun, H. *Angew. Chem., Int. Ed.* **2022**, *61*, No. e202203826.
(13) Zhong, L.; Chuan, J.; Gong, B.; Shuai, P.; Zhou, Y.; Zhang, Y.; Jiang, Z.; Zhang, D.; Liu, X. *Sci. China: Life Sci.* **2020**, *63*, 777.
(14) Lei, Q.; Li, Y.; Hou, H.; Wang, F.; Ouyang, Z.; Zhang, Y.; Lai, D.; Banga Ndzouboukou, N.; Xu, L.; Zhang, Z.; Chen, B.; Xue, H.; Lin, X. S.; Zheng, Y. X.; Yao, Z. J.; Wang, X. N.; Yu, C. Z.; Jiang, H. W.; Zhang, H. N.; Qi, H.; Guo, S. J.; Huang, S. H.; Sun, Z. Y.; Tao, S. C.; Fan, X. L. *Allergy* **2021**, *76*, 551−561.
(15) Xiang, J.; Yan, M.; Li, H.; Liu, T.; Lin, C.; Huang, S.; Shen, C. *medRxiv* **2020**, DOI: 10.1101/2020.02.27.20028787.
(16) GeurtsvanKessel, C. H.; Okba, N. M. A.; Igloi, Z.; Bogers, S.; Embregts, C. W. E.; Laksono, B. M.; Leijten, L.; Rokx, C.; Rijnders, B.; Rahamat-Langendoen, J.; van den Akker, J. P. C.; van Kampen, J. J. A.; van der Eijk, A. A.; van Binnendijk, R. S.; Haagmans, B.; Koopmans, M. *Nat. Commun.* **2020**, *11*, 3436.
(17) Van Honacker, E.; Coorevits, L.; Boelens, J.; Verhasselt, B.; Van Braeckel, E.; Bauters, F.; De Bus, L.; Schelstraete, P.; Willems, J.; Vandendriessche, S.; Padalko, E. *Acta Clin. Belg.* **2020**, *77*, 315.
(18) Gilboa, T.; Cohen, L.; Cheng, C.-A.; Lazarovits, R.; Uwamanzu-Nna, A.; Han, I.; Griswold, K., Jr.; Barry, N.; Thompson, D. B.; Kohman, R. E.; Woolley, A. E.; Karlson, E. W.; Walt, D. R. *Angew. Chem.* **2021**, *133*, 26170−26176.
(19) Liu, G.; Rusling, J. F. *ACS Sens* **2021**, *6*, 593−612.
(20) Heggestad, J. T.; Kinnamon, D. S.; Olson, L. B.; Liu, J.; Kelly, G.; Wall, S. A.; Oshabaheebwa, S.; Quinn, Z.; Fontes, C. M.; Joh, D. Y.; Hucknall, A. M.; Pieper, C.; Anderson, J. G.; Naqvi, I. A.; Chen, L.; Que, L. G.; Oguin, T.; Nair, S. K.; Sullenger, B. A.; Woods, C. W.; Burke, T. W.; Sempowski, G. D.; Kraft, B. D.; Chilkoti, A. *Sci. Adv.* **2021**, *7*, No. eabg4901.
(21) Liu, H.; Yang, A.; Song, J.; Wang, N.; Lam, P.; Li, Y.; Law, H. K.-w.; Yan, F. *Sci. Adv.* **2021**, *7*, No. eabg8387.
(22) Huber, M.; Kepesidis, K. V.; Voronina, L.; Božić, M.; Trubetskov, M.; Harbeck, N.; Krausz, F.; Žigman, M. *Nat. Commun.* **2021**, *12*, 1511.
(23) Zhang, L.; Xiao, M.; Wang, Y.; Peng, S.; Chen, Y.; Zhang, D.; Zhang, D.; Guo, Y.; Wang, X.; Luo, H.; Zhou, Q.; Xu, Y. *Anal. Chem.* **2021**, *93*, 2191−2199.
(24) Haldavnekar, R.; Venkatakrishnan, K.; Tan, B. *Nat. Commun.* **2018**, *9*, 3065.
(25) Martin, F. L.; Kelly, J. G.; Llabjani, V.; Martin-Hirsch, P. L.; Patel, I. I.; Trevisan, J.; Fullwood, N. J.; Walsh, M. J. *Nat. Protoc.* **2010**, *5*, 1748−1760.
(26) Erukhimovitch, V.; Talyshinsky, M.; Souprun, Y.; Huleihel, M.*DNA Viruses: Methods and Protocols*; Humana Press: Totowa, NJ, 2005; pp 161−172.
(27) Santos, M. C. D.; Nascimento, Y. M.; Araújo, J. M. G.; Lima, K. M. G. *RSC Adv.* **2017**, *7*, 25640−25649.
(28) Roy, S.; Perez-Guaita, D.; Bowden, S.; Heraud, P.; Wood, B. R. *Clinical Spectroscopy* **2020**, *1*, 100001.
(29) Salman, A.; Erukhimovitch, V.; Talyshinsky, M.; Huleihil, M.; Huleihel, M. *Biopolymers* **2002**, *67*, 406−412.
(30) Bahmani, M.; Khosravi, A.; Miri, Y.; Iwabu, K.; Ikuta, A.; Sakudo, A. *Mol. Med. Rep.* **2009**, *2*, 805−9.
(31) Wood, B. R.; Kochan, K.; Bedolla, D. E.; Salazar-Quiroz, N.; Grimley, S. L.; Perez-Guaita, D.; Baker, M. J.; Vongsvivut, J.; Tobin, M. J.; Bambery, K. R.; Christensen, D.; Pasricha, S.; Eden, A. K.; Mclean, A.; Roy, S.; Roberts, J. A.; Druce, J.; Williamson, D. A.; McAuley, J.; Catton, M.; Purcell, D. F. J.; Godfrey, D. I.; Heraud, P. *Angew. Chem.* **2021**, *133*, 17239−17244.
(32) Liu, H.; Dai, E.; Xiao, R.; Zhou, Z.; Zhang, M.; Bai, Z.; Shao, Y.; Qi, K.; Tu, J.; Wang, C.; Wang, S. *Sens. Actuators, B* **2021**, *329*, 129196.
(33) Barauna, V. G.; Singh, M. N.; Barbosa, L. L.; Marcarini, W. D.; Vassallo, P. F.; Mill, J. G.; Ribeiro-Rodrigues, R.; Campos, L. C. G.; Warnke, P. H.; Martin, F. L. *Anal. Chem.* **2021**, *93*, 2950−2958.
(34) Banerjee, A.; Gokhale, A.; Bankar, R.; Palanivel, V.; Salkar, A.; Robinson, H.; Shastri, J. S.; Agrawal, S.; Hartel, G.; Hill, M. M.; Srivastava, S. *Anal. Chem.* **2021**, *93*, 10391−10396.
(35) Yin, G.; Li, L.; Lu, S.; Yin, Y.; Su, Y.; Zeng, Y.; Luo, M.; Ma, M.; Zhou, H.; Orlandini, L.; Yao, D.; Liu, G.; Lang, J. *J. Raman Spectrosc.* **2021**, *52*, 949−958.
(36) Goulart, A. C. C.; Zangaro, R. A.; Carvalho, H. C.; Silveira, J. L. *J. Raman Spectrosc.* **2021**, *52*, 2671−2682.
(37) Nogueira, M. S.; Leal, L. B.; Marcarini, W.; Pimentel, R. L.; Muller, M.; Vassallo, P. F.; Campos, L. C. G.; dos Santos, L.; Luiz, W. B.; Mill, J. G.; Barauna, V. G.; de Carvalho, L. *Sci. Rep.* **2021**, *11*, 15409.
(38) Andersson, M. I.; Arancibia-Carcamo, C. V.; Auckland, K.; Baillie, J. K.; Barnes, E.; Beneke, T.; Bibi, S.; Brooks, T.; Carroll, M.; Crook, D.; Dingle, K.; Dold, C.; Downs, L. O.; Dunn, L.; Eyre, D. W.; Gilbert Jaramillo, J. J.; Harvala, H.; Hoosdally, S.; Ijaz, S.; James, T.; James, W.; Jeffery, K.; Justice, A.; Klenerman, P.; Knight, J. C.; Knight, M.; Liu, X.; Lumley, S. F.; Matthews, P. C.; McNaughton, A. L.; Mentzer, A. J.; Mongkolsapaya, J.; Oakley, S.; Oliveira, M. S.; Peto, T.; Ploeg, R. J.; Ratcliff, J.; Robbins, M. J.; Roberts, D. J.; Rudkin, J.; Russell, R. A.; Screaton, G.; Semple, M. G.; Skelly, D.; Simmonds, P.; Stoesser, N.; Turtle, L.; Wareing, S.; Zambon, M. *Wellcome Open Res.* **2020**, *5*, 181.
(39) Chen, Z.; Garcia, J. G.; Wirz, V.; Wirz, R. E. *Phys. Fluids* **2020**, *32*, 111702.
(40) Zhang, L.; Wang, H.; Luo, H. *Plasma Processes Polym.* **2020**, *17*, 1900197.
(41) Guo, Y.; Liu, P.; Zhang, L.; Peng, S.; Wang, X.; Luo, H.; Wu, G. *Appl. Phys. Lett.* **2021**, *119*, 090601.
(42) Zhang, L.; Guo, Y.; Chang, X.; Yao, Z.; Wei, X.; Feng, Z.; Zhang, D.; Zhou, Q.; Wang, X.; Luo, H. *J. Hazard. Mater.* **2022**, *435*, 129075.
(43) Tay, M. Z.; Poh, C. M.; Rénia, L.; MacAry, P. A.; Ng, L. F. P. *Nat. Rev. Immunol.* **2020**, *20*, 363−374.
(44) LeCun, Y.; Boser, B.; Denker, J. S.; Henderson, D.; Howard, R. E.; Hubbard, W.; Jackel, L. D. *Neural Comput.* **1989**, *1*, 541−551.
(45) Szymańska, E.; Saccenti, E.; Smilde, A. K.; Westerhuis, J. A. *Metabolomics* **2012**, *8*, 3−16.
(46) Yman, V.; Tuju, J.; White, M. T.; Kamuyu, G.; Mwai, K.; Kibinge, N.; Asghar, M.; Sundling, C.; Sondén, K.; Murungi, L.; Kiboi, D.; Kimathi, R.; Chege, T.; Chepsat, E.; Kiyuka, P.; Nyamako, L.; Osier, F. H. A. .; Färnert, A. *Nat. Commun.* **2022**, *13*, 331−15.
(47) Guo, Y.; Fang, M.; Zhang, L.; Sun, J.; Wang, X.; Tie, J.; Zhou, Q.; Zhang, L.; Luo, H. *Appl. Phys. Lett.* **2022**, *121*, 074101.
(48) Kim, D.; Jung, S.; Lee, S. *Clin. Med. Res.* **2018**, *9*, 5−6.
(49) Nie, M.; Zhang, W.; Xiao, M.; Luo, J.; Bao, K.; Chen, J.; Li, B. *J. Phytopathol.* **2007**, *155*, 364−367.
(50) Westerhuis, J. A.; Hoefsloot, H. C.; Smit, S.; Vis, D. J.; Smilde, A. K.; van Velzen, E. J.; van Duijnhoven, J. P.; van Dorsten, F. A. *Metabolomics* **2008**, *4*, 81−89.
(51) Galindo-Prieto, B.; Eriksson, L.; Trygg, J. *J. Chemom.* **2014**, *28*, 623−632.
(52) Xiling, G.; Yin, C.; Ling, W.; Xiaosong, W.; Jingjing, F.; Fang, L.; Xiaoyan, Z.; Yiyue, G.; Ying, C.; Lunbiao, C.; Liubo, Z.; Hong, S.; Yan, X. *Sci. Rep.* **2021**, *11*, 2418−9.
(53) Ho, C. S.; Jean, N.; Hogan, C. A.; Blackmon, L.; Jeffrey, S. S.; Holodniy, M.; Banaei, N.; Saleh, A. A. E.; Ermon, S.; Dionne, J. *Nat. Commun.* **2019**, *10*, 4927.
(54) Carbon-Mangels, M.; Hutter, M. C. *Mol. Inform.* **2011**, *30*, 885−895.